STRUCTURAL SCIENCE
CRYSTAL ENGINEERING
MATERIALS

ISSN 2052-5206

Sheared structure $Pb_4Sr_{14}Fe_{23}O_{52}$ solved by three-dimensional electron diffraction combined with atomic scale STEM imaging

Christophe Lepoittevin*

University of Grenoble Alpes, CNRS, Grenoble INP, Institut Néel, 38000 Grenoble, France. *Correspondence e-mail: christophe.lepoittevin@neel.cnrs.fr

Received 23 July 2026
Accepted 4 September 2026

Edited by J. Hadermann, University of Antwerp, Belgium

Keywords: crystal structure; 3D electron diffraction; HAADF and ABF STEM; ferrite.

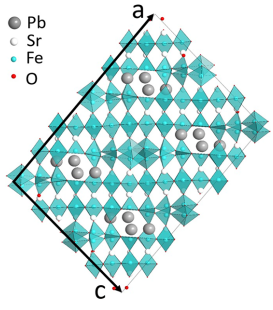
CCDC reference: 2585591

Supporting information: this article has supporting information at journals.iucr.org/b

Ferrite $Pb_4Sr_{14}Fe_{23}O_{52}$ was synthesized in 2006, and its structure was partially described from the interpretation of high-resolution transmission electron microscopy images. Twenty years later, thanks to the constant development in electron crystallography, the crystal structure of this oxide is fully determined by combining three-dimensional electron diffraction with aberration-corrected scanning transmission electron microscopy (STEM). The compound crystallizes in the monoclinic lattice, space group $C2/c$, with unit-cell parameters a = 34.782 (8) Å, b = 5.522 (2) Å, c = 24.962 (7) Å and β = 99.11 (2)°. The dynamically refined structure consists of the collapse of a single perovskite layer and an oxygen-deficient rock-salt-type layer. This work demonstrates the potential of combining electron crystallography and atomic resolution STEM imaging to solve complex oxide structures that remained inaccessible using earlier experimental approaches.

1. Introduction

Over the past fifteen years, three-dimensional electron diffraction (3D ED) has evolved into a powerful and routinely used technique for *ab initio* crystal structure determination (Gemmi *et al.*, 2019). This progress has been driven by major advances in electron microscopy instrumentation, including the development of fast and highly sensitive detectors, automated data acquisition protocols, and dedicated software for data processing and structure solution. The most commonly used programs are *PETS2* for the processing of precession ED tomography and continuous rotation ED data (Palatinus *et al.*, 2019), *XDS* for indexing, integration and scaling of diffraction intensities (Kabsch, 2010), *RED* for automated three-dimensional reciprocal space reconstruction and data processing (Wan *et al.*, 2013) and *DIALS*, which provides a robust framework for the processing of ED data, particularly in MicroED and serial electron crystallography applications (Clabbers *et al.*, 2018). These developments have greatly improved the accuracy, reliability and accessibility of 3D ED, enabling routine structure determination from crystals too small for conventional single-crystal X-ray diffraction. As a result, crystal structures that were previously inaccessible can now be routinely determined from submicrometric crystals. The capabilities of 3D ED have been demonstrated for a wide range of structurally complex materials, including zeolites (Örs *et al.*, 2024; Li *et al.*, 2024; Tirado *et al.*, 2025*a*; Tirado *et al.*, 2025*b*), metal–organic frameworks (Huang *et al.*, 2021; Gorelik *et al.*, 2026), and both commensurately and incommensurately modulated structures (Mei *et al.*, 2023; Plana-Ruiz *et al.*, 2024).



OPEN ACCESS
Published under a CC BY 4.0 licence

Before the widespread adoption of automated 3D ED methods, ED data had already been used for quantitative crystal structure analysis, including structure solution and refinement from two-dimensional diffraction patterns. Several approaches have been developed to extract structural information from such data, including direct methods and least-squares refinement procedures using electron scattering factors. In particular, the MSLS (MultiSlice Least-Squares) approach enabled quantitative structure refinement from dynamical ED patterns by explicitly taking multiple scattering into account (Jansen *et al.*, 1998). Structure solution and refinement from ED data had therefore already been demonstrated before the emergence of modern 3D ED workflows. The main advance brought by modern 3D ED was not the possibility of extracting structural information from ED itself, but rather the development of experimental and computational workflows that allow substantially more complete three-dimensional reciprocal space datasets to be collected and processed in a systematic and increasingly automated manner. Earlier approaches were often based on a limited number of two-dimensional diffraction patterns recorded along selected zone axes and could require more specialized data collection, processing and refinement strategies. In addition, the strong influence of dynamical scattering on ED intensities could complicate quantitative structure analysis, particularly for thicker crystals. Nevertheless, dynamical refinement methods had already demonstrated that reliable structural information could be extracted from ED

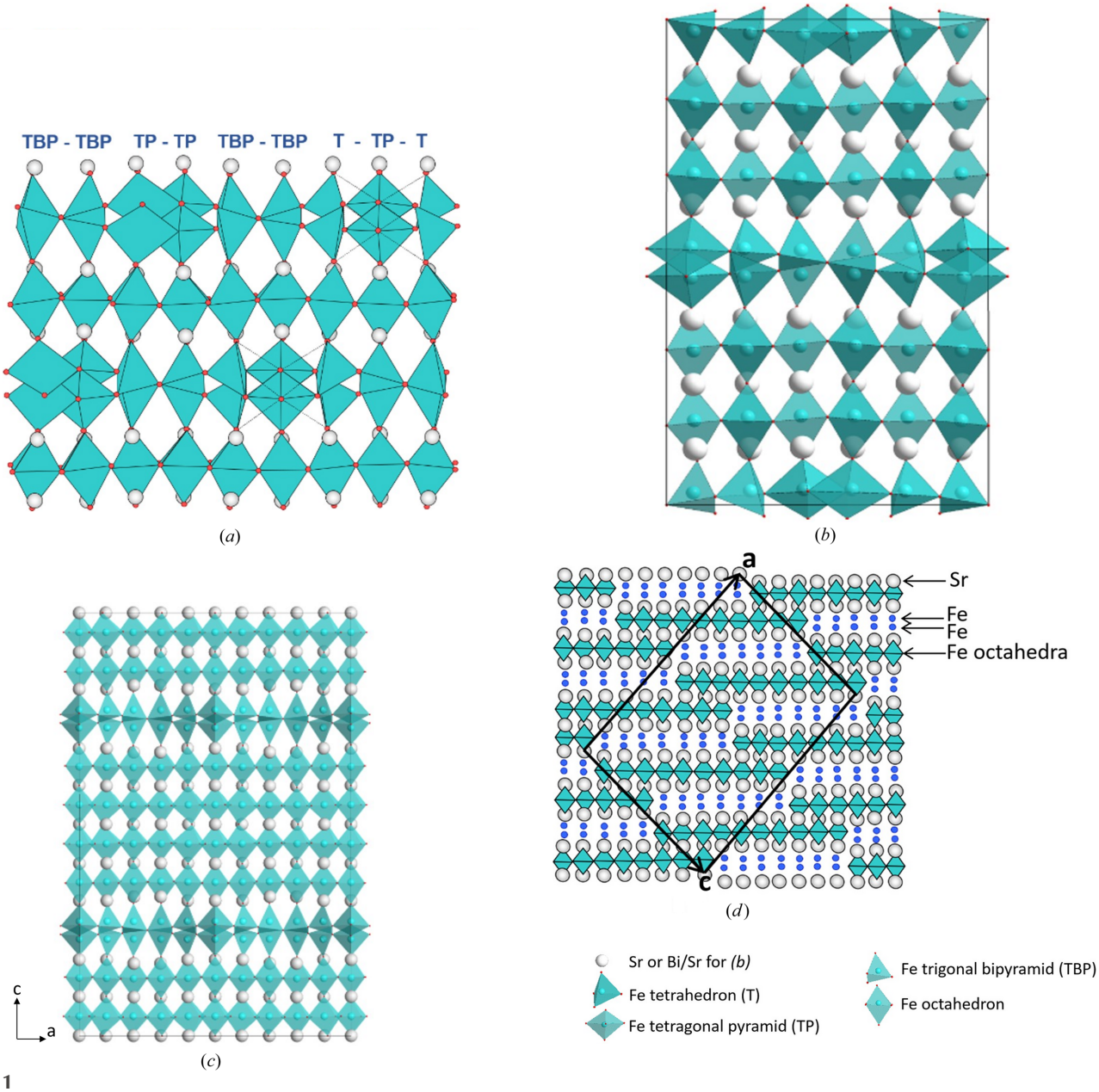


Figure 1
Structures of (*a*) $Sr_4Fe_6O_{13-\delta}$, (*b*) $(BiSr_{3.5})Fe_6O_{14}$, (*c*) $(Tl_\varepsilon Sr_{5-\varepsilon})Fe_6O_{15.4}$ and (*d*) first structural model of so-called '$Pb_4Sr_{13}Fe_{24}O_{53}$' deduced by zone axis ED and HRTEM images interpretation in 2006.

data when multiple scattering was explicitly considered (Jansen *et al.*, 1998). The subsequent development of automated 3D ED acquisition and processing has made such analyses considerably more accessible and has facilitated the routine determination of increasingly complex crystal structures. However, the structural complexity of some compounds may require the combination of single-crystal X-ray diffraction and ED to achieve a reliable structure determination. A representative example is the complex incommensurately modulated $KNd(MoO_4)_2$ (Zhou *et al.*, 2016). Moreover, because electrons interact with the electrostatic potential rather than the electron density, ED is particularly sensitive to light atoms, making it possible to locate O and even H atoms that are often difficult to detect by conventional X-ray diffraction (Palatinus *et al.*, 2017; Klar *et al.*, 2023; Yörük *et al.*, 2025). Consequently, numerous compounds whose structures could not previously be solved because of crystal size limitations or structural complexity have recently become accessible to complete crystallographic characterization.

In this context of complex structures, the layered ferrites belonging to the homologous series $[Sr_2Fe_4O_{7-\delta}][Sr_2Fe_2O_6]_m$, consist of the periodic intergrowth of one oxygen-deficient rock-salt-type layer and m perovskite layers. The parent member (m = 1), $Sr_4Fe_6O_{13-\delta}$ [Fig. 1(*a*)] exhibits an incommensurately modulated structure originating from the distribution of oxygen vacancies within the rock-salt-type layer. The modulated feature of this structure was identified by single-crystal X-ray diffraction study, which showed three different environments of Fe in the oxygen-deficient rock-salt-type layer: trigonal bipyramid (TBP), tetragonal pyramid (TP) and tetrahedron (T) (Mellenne *et al.*, 2004; Pérez *et al.*, 2006). Partial substitution of Sr^{2+} by stereochemically active cations such as Bi^{3+} or Tl^{+} stabilizes the m = 2 [Fig. 1(*b*)] and m = 4 [Fig. 1(*c*)] members of the series, corresponding to the compositions $(BiSr_{3.5})Fe_6O_{14}$ (Lepoittevin *et al.*, 2004; Grebille *et al.*, 2006) and $(Tl_\varepsilon Sr_{5-\varepsilon})Fe_6O_{15.4}$ (Lepoittevin, 2016). These two structures were solved using single-crystal X-ray diffraction and 3D ED, respectively, and in contrast to the parent phase, they exhibit commensurate modulation that can be described using well defined superstructures. Motivated by the possibility of stabilizing new members of this family through cation substitution, the solid solution $(Sr_{4-x}Pb_x)Fe_6O_{13\pm\delta}$ was subsequently investigated (Lepoittevin *et al.*, 2006). For x = 0.7, a previously unknown phase was isolated and identified as a new lead-substituted ferrite. At the time, the complete crystallographic characterization of this complex structure from ED remained challenging because of the limited reciprocal space coverage provided by two-dimensional diffraction data and the need to account for dynamical scattering. A preliminary structural model, established from high-resolution transmission electron microscopy (HRTEM), selected area ED, and energy-dispersive X-ray (EDX) spectroscopy, indicated that this phase originated from the shearing of a single perovskite layer and an oxygen-deficient rock-salt-type layer [Fig. 1(*d*)]. Although this study successfully described the overall structural framework, essential crystallographic information remained inaccessible, particularly the distribution of the Pb atoms and the arrangement of O atoms within the oxygen-deficient rock-salt-type layer.

In the present work, we revisit this compound using the current state of the art electron crystallography toolbox. By combining *ab initio* structure solution from 3D ED with aberration-corrected HAADF and annular bright-field (ABF) STEM imaging and dynamical refinement, we establish the complete crystal structure of $Pb_4Sr_{14}Fe_{23}O_{52}$.

2. Experimental

2.1. Synthesis

The single-phase powder was synthesized under an inert atmosphere in a glove box using PbO, SrO, SrO_2 and Fe_2O_3 as starting materials. SrO was obtained by thermal decomposition of $Sr(OH)_2{\cdot}8H_2O$ at 1100 °C and subsequently maintained at this temperature until use to prevent hydration. The precursor powders were weighed according to the nominal stoichiometric composition and thoroughly homogenized by grinding in an agate mortar. The resulting powder mixture was uniaxially pressed into bar-shaped pellets, sealed in an evacuated silica tube, and subjected to a heat treatment at 1100 °C for 48 h. The heating and cooling steps were both performed at a controlled rate of 1.5 °C min^{-1}.

2.2. Transmission electron microscopy (TEM)

The TEM specimen was prepared by dispersing a small amount of powder in ethanol and depositing a drop of the suspension onto a holey carbon-coated copper grid. 3D ED and STEM analyses were performed on a probe-corrected Jeol NEOARM 200F microscope operating at 200 kV, equipped with a Nanomegas Digistar precession device and a 4K CMOS Gatan OneView camera. Atomic scale chemical contrast imaging was performed using high-angle annular dark field (HAADF) and ABF detectors in STEM mode. Stepwise ED tomography data were collected using a ±70° tomography specimen holder, using 1° increments and a 1.2° precession angle to ensure full integration of diffracted intensities (Mugnaioli *et al.*, 2009). Data analysis and 3D reciprocal space reconstruction were conducted in *PETS2* (Process Electron Tilt Series, version 2) software (Palatinus *et al.*, 2019). The structural model was calculated using the charge flipping algorithm (Palatinus, 2013) implemented in *Superflip* (Palatinus & Chapuis, 2007) and subsequently kinematically and dynamically refined in *JANA2020* (Petříček *et al.*, 2023).

3. Results

3.1. Unit-cell and structural model determination

A 3D ED dataset was collected on an isolated single crystallite selected to avoid any overlap with neighbouring particles throughout the entire tilt series. Prior to diffraction data acquisition, the crystal composition was assessed using EDX, confirming the presence of Pb, Sr and Fe with approximate atomic proportions of 10%, 40% and 50%, respectively. These values are consistent with the targeted Pb–Sr ferrite phase and

were used to verify the chemical homogeneity of the selected crystal. The diffraction dataset was acquired over an angular range from +60° to −60°. To ensure that diffraction intensities originated from the same crystal volume during the complete rotation experiment, a 20 µm selected area aperture was employed, allowing the illuminated region to remain confined to the same area of the crystallite throughout the data collection. The 121 ED frames were processed using *PETS2* software. Diffraction spots were first automatically detected and indexed throughout the tilt series. From these data, *PETS2* determined the experimental rotation axis, giving rise to the sinogram shown in Fig. 2(*a*). The software then reconstructed the three-dimensional reciprocal space, enabling the determination of the unit-cell parameters and the crystal orientation, which was subsequently refined during the data reduction procedure. The refined unit cell was found to be monoclinic, with the unit-cell parameters a = 34.782 (8) Å, b = 5.522 (2) Å, c = 24.962 (7) Å and β = 99.11 (2)°. Using the resulting orientation matrix, reflection intensities were extracted from each diffraction frame. During the data reduction procedure, *PETS2* performs several refinements and corrections to improve the internal consistency of the dataset. These include refinement of the beam centres on individual diffraction patterns, correction of the experimental tilt angles, compensation for geometrical distortions of the diffraction frames, and refinement of both the orientation matrix and the unit-cell parameters. The quality of the processed data was assessed through the rocking curve representation, commonly called the camel plot [Fig. 2(*b*)]. This plot provides a graphical evaluation of the reflection intensity profiles and constitutes a reliable indicator of the quality of the dataset for subsequent *ab initio* structure determination and structure dynamical refinement.

Selected sections of the reciprocal lattice were calculated in order to analyse the reflection conditions and identify the compatible space groups. These sections, depicted in Fig. 3, reveal the systematic extinction condition $h + k = 2n$ for the general reflections *hkl*, which is consistent with a *C* centering. In addition, the *h*0*l* section exhibits the extinction condition $l = 2n$, indicating the presence of a *c* glide mirror perpendicular to the *b* axis. These conditions limiting the reflections are compatible with the monoclinic space groups *C*2/*c* and *Cc*. Following the final integration of the diffraction intensities, *PETS2* generated two reflection files: a conventional *hkl* file for *ab initio* structure resolution and a second for subsequent dynamical refinement. During the data reduction procedure, several Laue classes were evaluated, and the monoclinic 2/*m* symmetry was retained as it yielded the lowest merging residual $R_{\rm int}$.

The structural model was calculated from the integrated reflection intensities exported by *PETS2*. The dataset used for the structure solution comprised 6862 independent reflections, corresponding to a completeness of 87% up to a resolution of 0.70 Å. The charge flipping calculation successfully converged toward an initial electrostatic potential distribution, providing a first structural model of the investigated Pb–Sr ferrite. The solution was obtained with an agreement factor of 30.71% in space group *C*2/*c*.

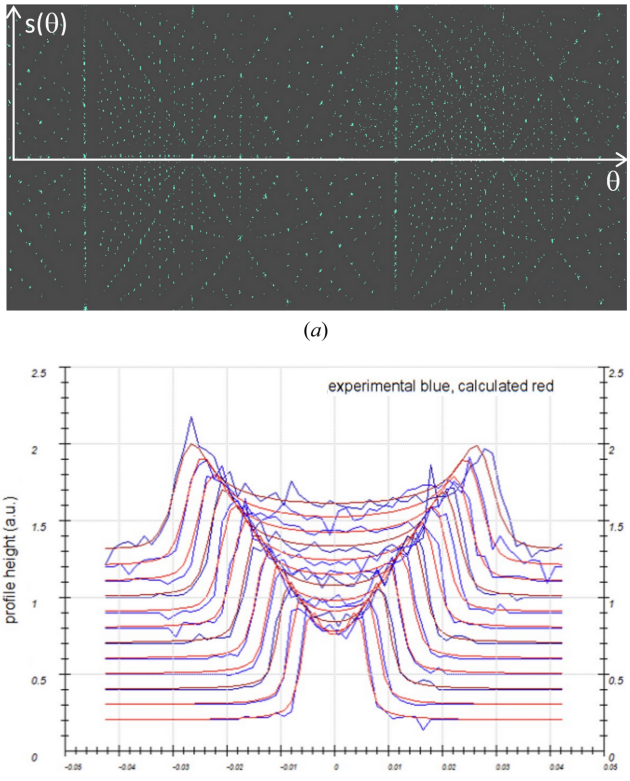


Figure 2
(*a*) Sinogram representing $s(\theta)$ (reflection position) versus θ (rotation angle) and (*b*) the camel plot after *PETS2* processing.

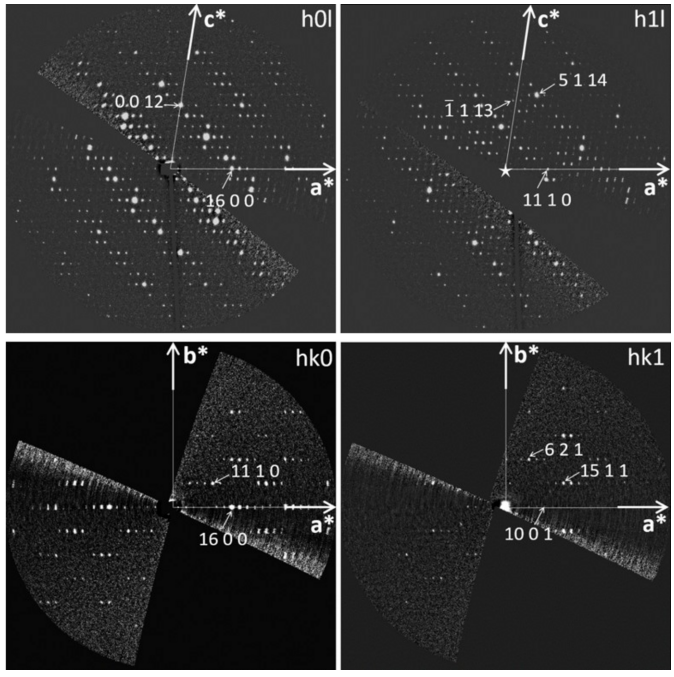


Figure 3
Selected sections of the reciprocal space exhibiting reflections indexing consistent with the space groups *C*2/*c* and *Cc*.

The resulting structural model presented in Fig. 4(*a*) closely resembles the first one reported in 2006. It consists of a framework built up from the collapse of single perovskite layers alternating with rock-salt-type oxygen-deficient double iron layers. The main features of the framework are therefore correctly reproduced by the charge flipping solution, confirming the validity of the structural model derived from the 3D ED data. However, this first model remains incomplete: several O atoms are absent, particularly within the oxygen-deficient double iron layers. Furthermore, the Pb and Sr cations appear to be randomly distributed over the same crystallographic sites, preventing an unambiguous assignment of their occupancies at this stage of the structure determination. This observation can be explained by comparison of electron and X-ray scattering factors of Pb, Sr and Fe over the same scattering vector range $0 \leq Q$ (Å^{-1}) ≤ 0.7. Based on values from Doyle & Turner (1968), X-ray scattering factors are, to a first approximation, proportional to the atomic number Z. Consequently, the large difference between Z(Pb) = 82 and Z(Sr) = 38 results in a pronounced separation of their X-ray scattering factors [Fig. 5(*a*)], making the two elements readily distinguishable. On the other hand, the difference between their electron scattering factors is much less pronounced over the same Q range [Fig. 5(*b*)]. The distinction between Pb and Sr is more directly visualized in HAADF-STEM images, owing to a strong dependence on atomic number Z. In order to search for the information of Pb/Sr and O atoms distribution in the structure, atomic scale STEM imaging was then employed.

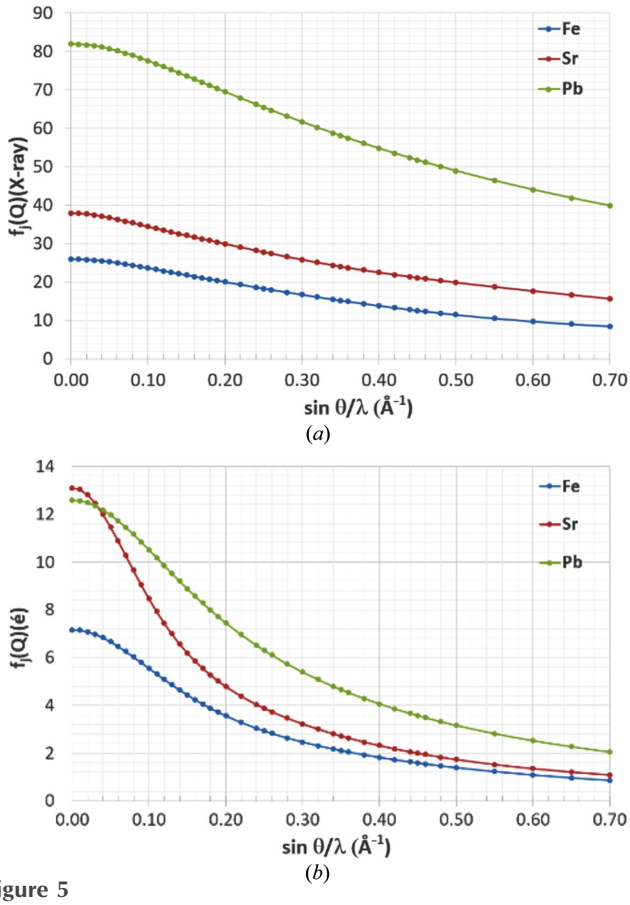


Figure 5
(*a*) X-ray and (*b*) electron scattering factor curves of Fe, Sr and Pb atoms plotted using values from Doyle & Turner (1968).

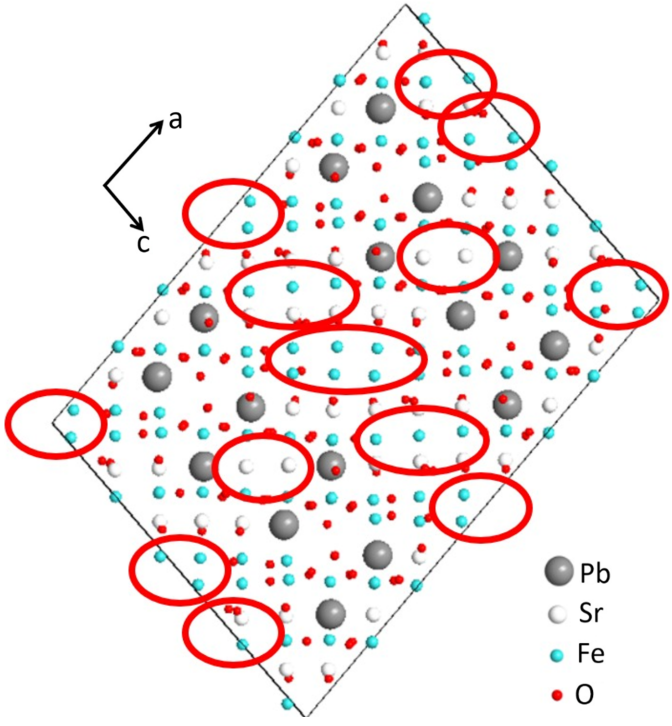
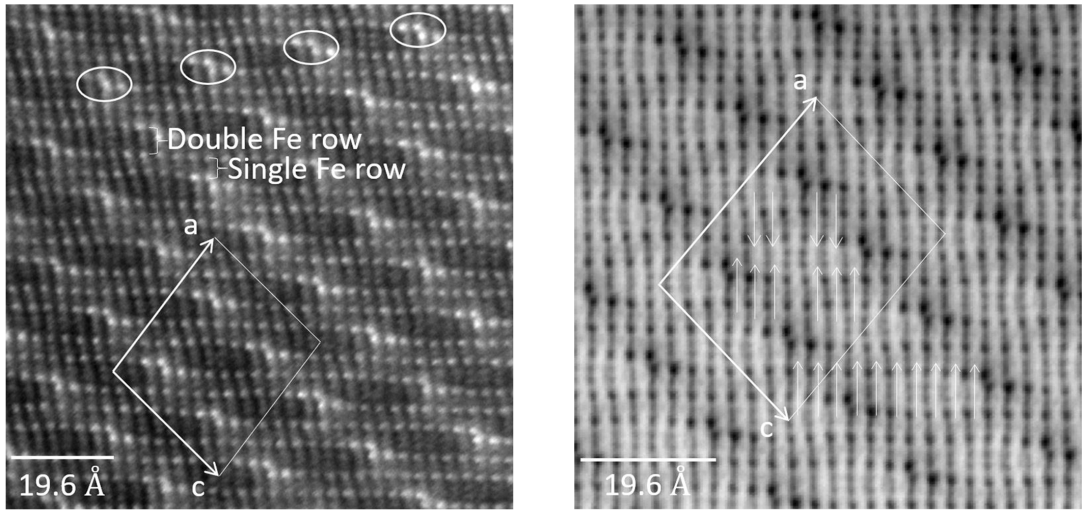


Figure 4
Raw structural model calculated by *Superflip*. The regions circled in red correspond to missing O atoms.

3.2. HAADF and ABF STEM

HAADF and ABF STEM provide complementary structural information. In HAADF STEM imaging, the contrast is approximately proportional to Z^n with $n \simeq 2$ (Pennycook *et al.*, 2000), producing a contrast in which heavy elements appear significantly brighter than lighter ones. This imaging mode is particularly suitable for identifying the distribution of heavy cations such as Pb (Z = 82), Sr (Z = 38) and Fe (Z = 26). In contrast, ABF STEM collects electrons scattered at lower angles, and the image contrast arises from the interference between the transmitted and diffracted electron beams. Consequently, the contrast does not follow a simple dependence on the atomic number but is also influenced by factors such as specimen thickness, crystal orientation and defocus. Under suitable imaging conditions, ABF STEM enables the direct visualization of light element atomic columns, such as oxygen.

Fig. 6(*a*) exhibits an HAADF STEM image acquired along the [010] zone axis. On this image, the Pb atomic columns are clearly identified as the brightest dots. They appear as groups of four atomic columns arranged in a characteristic staircase like configuration, directly revealing the displacement of the perovskite blocks responsible for the sheared nature of the structure. This observation provides direct experimental evidence that the Pb cations are intimately associated with the



(*a*) (*b*)

Figure 6
(*a*) [010]-oriented HAADF STEM image. White circles highlight Pb atomic columns. (*b*) [010]-oriented ABF STEM image, where oxygen atomic columns are pointed out by white arrows.

collapse mechanism. Such a collapse of layered frameworks induced by the incorporation of stereochemically active heavy cations is not unprecedented and has been previously reported in several complex oxides containing Bi^{3+} or Pb^{2+}. In particular, Bi-based layered oxides have been shown to undergo shear-induced structural rearrangements leading to sheared structures, where the stereochemical activity of the Bi $6s^2$ lone pair promotes distortions of the interlayer regions and stabilizes displaced perovskite blocks (Hervieu *et al.*, 1995; Hervieu *et al.*, 1997). The image also shows dots with slightly lower intensity assigned to Sr. Between the Sr layers, the Fe atoms are also clearly visible, despite their weaker contrast. The iron sublattice is organized into two distinct structural motifs: single rows composed of 11 Fe atomic columns and oxygen-deficient double rows systematically consisting of six pairs of Fe columns. These two arrangements alternate throughout the structure and are consistent with the layered framework deduced from structure solution, in which perovskite-like slabs alternate with oxygen-deficient rock-salt-type double Fe layers.

The [010] ABF STEM image provides complementary information on the oxygen sublattice [Fig. 6(*b*)]. Although the oxygen atomic columns exhibit a weak contrast barely distinguishable from the background, they can nevertheless be identified in both the single and double iron layers. Within the single Fe layers, O atoms are observed between Fe atoms. In double iron layers, pairs of oxygen atoms are adjacent to four pairs of Fe atoms, whereas only a single oxygen column is observed on each side of the double iron layer. All oxygen positions already present in the calculated structural model are consistent with the contrast observed in the ABF STEM image. ABF observations also offer valuable guidance for locating the O atoms that remain absent from the structural model. In the subsequent refinement procedure, these observations will be systematically compared with difference fast Fourier transform (FFT) maps calculated after each refinement cycle, allowing the missing oxygen sites to be identified and incorporated into the model.

3.3. Structure refinement

Based on the information obtained from the HAADF STEM image, the Pb atomic positions were reassigned to match the experimentally observed cation distribution. In particular, the staircase-like arrangement of Pb columns, directly visualized by Z contrast imaging, enabled an unambiguous distinction between Pb and Sr crystallographic sites. A kinematical refinement of the modified structural model was subsequently performed. This refinement served as the basis for the calculation of difference FFT maps in order to reveal positive residual electrostatic potential and locate missing atomic positions, particularly those corresponding to O atoms. As shown in Fig. 7, numerous positive residual maxima are observed in regions where O atoms are expected according to the ABF STEM observations. The agreement between these residual electrostatic potentials and the oxygen columns identified in the ABF confirm that these maxima correspond to missing oxygen sites. Consequently, O atoms were progressively introduced at these positions, leading to a more complete structural model.

After having completed the structural model, a full refinement was carried out using the dynamical theory of ED (Palatinus *et al.*, 2015). In contrast to the kinematical approximation, the dynamical refinement accounts for multiple scattering effects and precession motion, providing a significantly more accurate description of the interaction between the electron beam and the crystal. As expected, this resulted in a substantial improvement of the agreement between calculated and experimental diffraction intensities. In particular, the observed reliability factor, R_{obs}, was reduced by

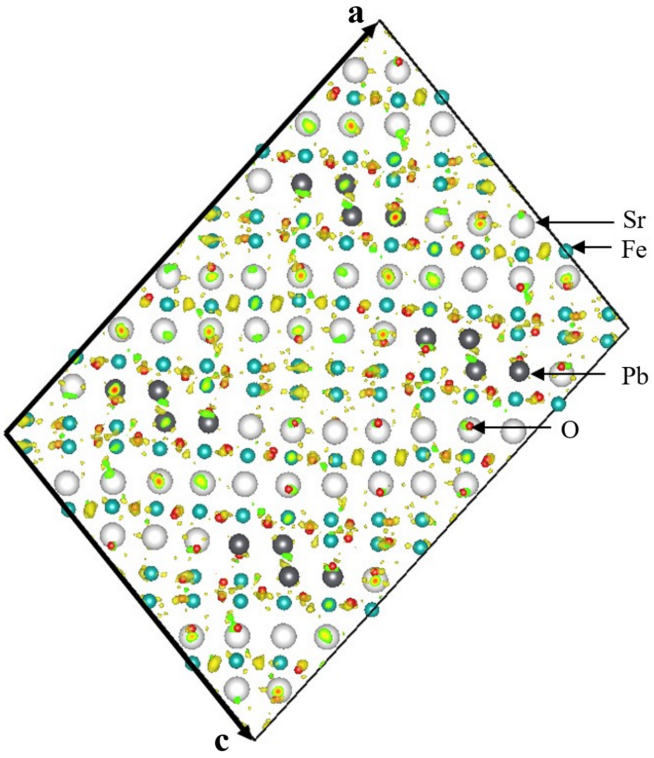


Figure 7
Difference FFT map created after kinematical refinement. Residual positive electrostatic potentials (yellow dots) reveal the positions of the last missing O atoms in the structure.

approximately a factor of 2.5 compared with the value obtained from the kinematical refinement. To assess the completeness of the final structural model, a last difference FFT map was calculated after convergence of the dynamical refinement. The remaining residual peaks are attributed to background noise, as they exhibit insufficient intensity to justify the introduction of new atoms [Fig. S1(*a*)]. Furthermore, several of these weak maxima are located at chemically unrealistic distances from the atoms already present in the refined structure, excluding their interpretation as physically meaningful atomic sites [Fig. S1(*b*)]. The absence of significant residual features therefore confirms that the final structural model provides a complete and self-consistent description of the crystal structure. The crystallographic parameters of the final structural model, including the refined unit-cell parameters, space group, atomic coordinates and atomic displacement parameters are summarized in Table 1. The reliability factors together with the parameters of the dynamical refinement are also reported. Slightly negative ADPs are obtained for O5, O9, O18 and O24. These values should not be interpreted as physically meaningful negative atomic displacements, but rather as an indication that the corresponding displacement parameters are poorly defined within the refinement. Their proximity close to zero probably reflects the limited precision with which the ADPs of light atoms can be determined from 3D ED data. Similar anomalous ADPs, including negative values, have been reported in 3D ED refinements and were shown to be sensitive to the quality and processing of the ED data (Yang *et al.*, 2022).

Table 1
Refined structural parameters based on 3D ED data performed in space group *C*2/*c*.

Space group *C*2/*c* (No. 15)
a = 34.782 (8) Å, b = 5.522 (2) Å, c = 24.962 (7) Å, β = 99.11 (2)°

Kinematical refinement
R(obs) = 31.26%, R(all) = 35.63%, wR(all) = 56.54%, GoF(obs) = 2.35, meas./obs. [$I > 3\sigma(I)$] reflections = 4603/2032
261 refined parameters

Dynamical refinement
R(obs) = 11.95%, R(all) = 39.46%, wR(all) = 12.17%, GoF(obs) = 4.06, meas./obs. [$I > 3\sigma(I)$] reflections = 8671/1222
318 refined parameters
g_{max}(Å^{-1}) = 1.45, $S_{g,max}$ (Å^{-1}) = 0.01, $R_{S_{g,max}}$ = 0.2, steps = 110

Atom label	Wyckoff	x	y	z	U_{iso}/U_{eq}(Å^2)
Pb1	8*f*	0.2348 (2)	0.495 (2)	0.2837 (3)	0.103 (4)†
Pb2	8*f*	0.2966 (1)	0.994 (2)	0.3674 (2)	0.049 (3)†
Sr1	8*f*	0.3531 (2)	0.513 (3)	0.4540 (3)	0.012 (2)
Sr2	8*f*	0.3398 (2)	0.991 (2)	0.6272 (3)	0.014 (2)
Sr3	8*f*	0.4680 (2)	0.509 (3)	0.6221 (3)	0.017 (2)
Sr4	8*f*	0.4096 (2)	0.984 (3)	0.5387 (3)	0.013 (2)
Sr5	8*f*	0.5298 (2)	0.978 (2)	0.7020 (3)	0.014 (2)
Sr6	8*f*	0.2799 (3)	0.497 (2)	0.5412 (4)	0.021 (2)
Sr7	8*f*	0.4050 (2)	0.506 (2)	0.7128 (3)	0.016 (2)
Fe1	8*f*	0.5107 (3)	0.072 (3)	0.5619 (4)	0.021 (3)
Fe2	8*f*	0.4554 (3)	0.424 (3)	0.4833 (4)	0.015 (3)
Fe3	8*f*	0.2593 (2)	0.499 (3)	0.4075 (4)	0.011 (3)
Fe4	8*f*	0.1024 (2)	0.571 (3)	0.1084 (4)	0.006 (2)
Fe5	8*f*	0.4286 (3)	0.572 (3)	0.3555 (4)	0.022 (3)
Fe6	8*f*	0.3164 (3)	0.003 (4)	0.4957 (4)	0.025 (3)
Fe7	8*f*	0.4353 (2)	0.999 (4)	0.6679 (3)	0.021 (3)
Fe8	8*f*	0.1998 (3)	0.005 (4)	0.3200 (4)	0.021 (3)
Fe9	8*f*	0.1398 (2)	0.477 (3)	0.2330 (4)	0.015 (2)
Fe10	8*f*	0.3354 (3)	0.466 (4)	0.3015 (5)	0.057 (4)
Fe11	8*f*	0.3752 (2)	0.495 (3)	0.5865 (4)	0.013 (3)
Fe12	4e	0.5	0.508 (5)	0.25	0.030 (4)
O1	8*f*	0.3493 (7)	0.280 (7)	0.538 (1)	0.032 (8)
O2	8*f*	0.2300 (6)	0.739 (6)	0.3518 (9)	0.015 (6)
O3	8*f*	0.1325 (5)	0.668 (5)	0.1701 (7)	0.022 (5)
O4	8*f*	0.3480 (5)	0.751 (5)	0.5419 (8)	0.001 (5)
O5	8*f*	0.4086 (4)	0.255 (4)	0.6319 (7)	−0.006 (4)
O6	8*f*	0.1007 (5)	0.520 (6)	0.2700 (8)	0.025 (6)
O7	8*f*	0.2402 (7)	0.254 (8)	0.349 (2)	0.06 (1)
O8	8*f*	0.1757 (6)	0.252 (5)	0.2629 (8)	0.012 (5)
O9	8*f*	0.2899 (4)	0.260 (4)	0.4470 (7)	−0.008 (4)
O10	8*f*	0.4133 (5)	0.403 (5)	0.4103 (7)	0.018 (5)
O11	8*f*	0.2888 (6)	0.763 (7)	0.447 (1)	0.020 (7)
O12	8*f*	0.5582 (4)	0.116 (5)	0.6177 (7)	0.012 (4)
O13	8*f*	0.4635 (7)	0.098 (8)	0.493 (1)	0.061 (9)
O14	8*f*	0.5287 (7)	0.232 (6)	0.287 (1)	0.020 (5)
O15	8*f*	0.5319 (7)	−0.247 (7)	0.297 (1)	0.021 (6)
O16	8*f*	0.5989 (6)	0.231 (5)	0.3799 (9)	0.022 (6)
O17	8*f*	0.5369 (6)	0.497 (7)	0.1893 (9)	0.028 (7)
O18	8*f*	0.3369 (4)	0.456 (4)	0.6310 (6)	−0.004 (4)
O19	8*f*	0.2815 (6)	0.981 (4)	0.5500 (8)	0.018 (5)
O20	8*f*	0.3782 (6)	0.368 (6)	0.815 (1)	0.045 (7)
O21	8*f*	0.4903 (7)	0.420 (8)	0.947 (1)	0.08 (1)
O22	8*f*	0.6754 (8)	0.762 (8)	0.763 (2)	0.07 (1)
O23	8*f*	0.5224 (6)	−0.015 (8)	0.8986 (9)	0.027 (6)
O24	8*f*	0.5778 (3)	0.534 (4)	0.9694 (6)	−0.009 (3)
O25	8*f*	0.1918 (4)	0.021 (5)	0.1469 (6)	0.001 (4)
O26	8*f*	0.1375 (5)	0.503 (6)	0.0628 (8)	0.027 (6)

† Anisotropic ADPs were refined for Pb1 and Pb2.

4. Final structure and discussion

4.1. Structure description

The final structure, depicted in Fig. 8, corresponds to the chemical composition $Pb_4Sr_{14}Fe_{23}O_{52}$ and consists of a periodic alternation of two distinct structural blocks. The first block is a perovskite-like layer containing nine Fe atoms, all in octahedral environment. This slab alternates with an oxygen-deficient rock-salt-type layer composed of six pairs of Fe atoms exhibiting a variety of coordination environments arising from the ordered distribution of oxygen vacancies. Within this layer, the Fe atoms are found in tetrahedral (T), tetragonal pyramidal (TP) and trigonal bipyramidal (TBP) environments, following the ordered sequence TP-T-TBP-TBP-T-TP. The main feature of this structure is the periodic collapse of these two slabs, directly associated with the incorporation of Pb atoms. As shown by HAADF STEM imaging and confirmed by the dynamical refinement, a block of four Pb atoms adopt a characteristic staircase-like arrangement, producing a displacement of $-\frac{1}{10}\mathbf{a} + \frac{1}{7}\mathbf{c}$ of adjacent Fe single layers, giving rise to the sheared structure. The stereochemical influence of Pb is reflected in the local coordination of the neighbouring Fe atoms, since those immediately above and below a pair of Pb systematically adopt a square pyramidal environment. The representation of the different Fe environments with the corresponding Fe–O distances is displayed in Fig. 9. To further assess the local coordination environments of the Fe atoms, bond valence sum (BVS) calculations were performed using the final refined structural model. The BVS method estimates the oxidation state of each Fe site from its coordination number and the corresponding Fe–O bond distances. The bond valence s_{ij} was calculated according to the expression proposed by Brown & Altermatt (1985):

$$s_{ij} = \sum_i N_i \exp\left(\frac{r_0 - r_{ij}}{B}\right),$$

where N_i is coordination number, r_{ij} is the metal–ligand distance, r_0 and B are empirical parameters. Values of r_0 and B used for our calculations are the ones reported for Fe–O bonds by Kanowitz & Palenik (1998). The estimated BVSs for the individual Fe sites are summarized in Table 2. Overall, the calculated values indicate that the majority of the Fe atoms exhibit an oxidation state around Fe^{3+}, except for Fe8, for which the calculated BVS is closer to 2, indicating an oxidation state approaching Fe^{2+}. This site corresponds to the Fe atom located in a square pyramidal coordination environment, immediately above and below a pair of Pb atoms. By considering these oxidation states for Fe, as well as conventional +2 for Pb/Sr and −2 for O, the charge neutrality is yielded in agreement with the chemical composition $Pb_4Sr_{14}Fe_{23}O_{52}$.

Another feature of the structure is the corrugation of the layers. Rather than being perfectly planar, both the perovskite

Table 2
Estimated oxidation states of the independent Fe sites obtained from BVS calculations in the refined structure of $Pb_4Sr_{14}Fe_{23}O_{52}$.

Fe1	Fe2	Fe3	Fe4	Fe5	Fe6	Fe7	Fe8	Fe9	Fe10	Fe11	Fe12
3.1	2.8	2.8	2.9	3.1	2.8	2.9	2.3	3.2	3.2	3.5	2.8

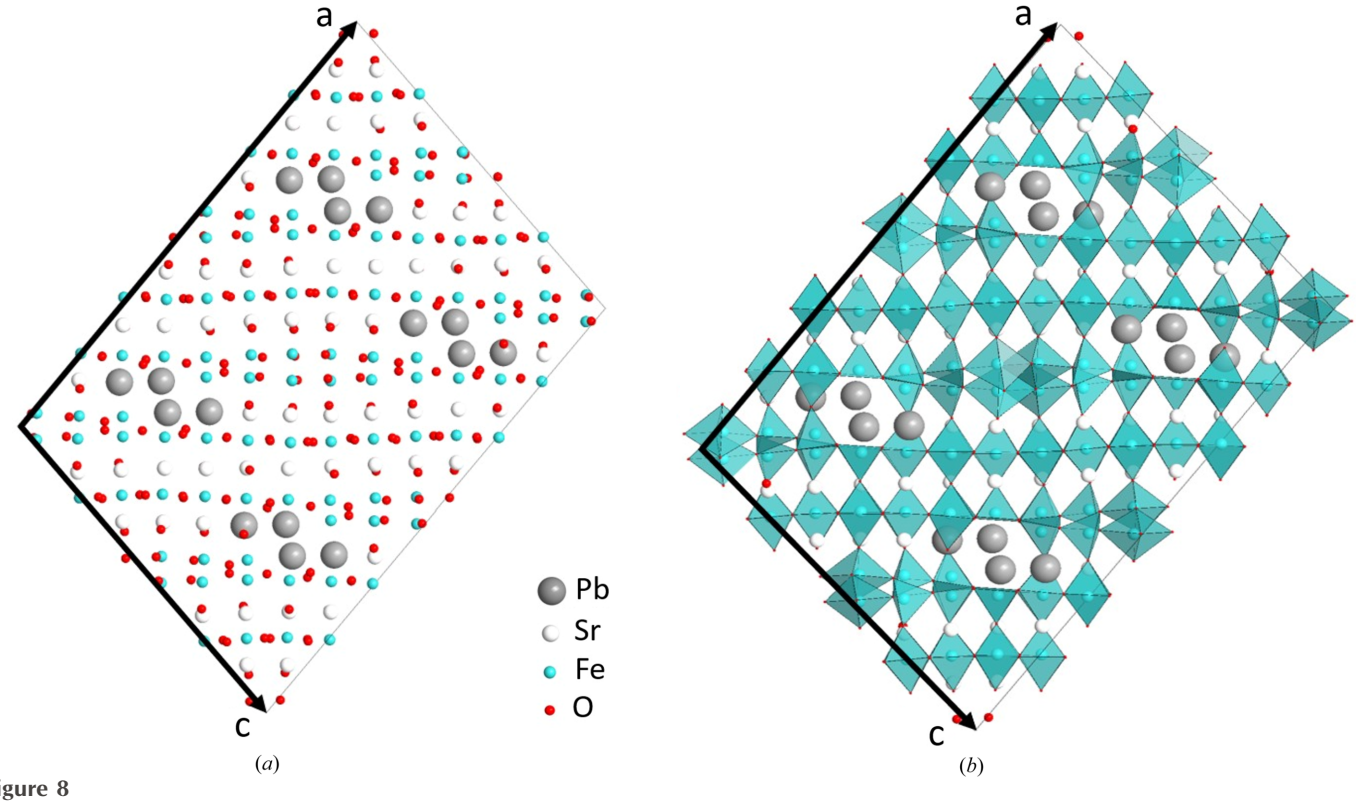


Figure 8
Refined structure projected along [010] direction (*a*) without and (*b*) with Fe coordination polyhedra.

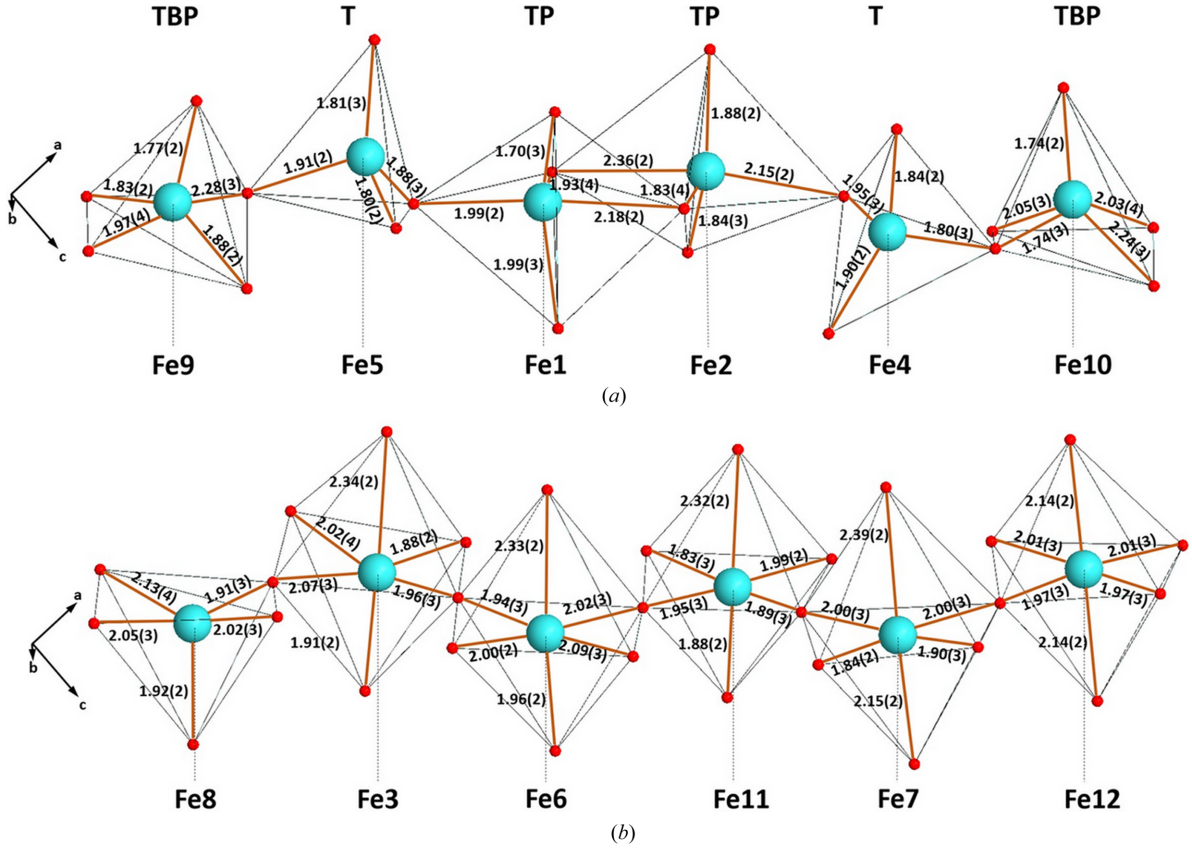


Figure 9
Representation of the Fe environments and Fe–O distances in the (*a*) oxygen-deficient rock-salt-type layer (TP = tetragonal pyramid, TBP = trigonal bipyramid and T = tetrahedron) and (*b*) perovskite-type layer.

and oxygen-deficient rock-salt-type layers exhibit a periodic undulation throughout the structure. This distortion originates from the ordered oxygen distribution within the rock-salt-type layer. The central part of the layer, with the tetragonal pyramids, is significantly larger than its outer regions, which contain tetrahedra and trigonal bipyramids. This geometrical variation is directly transmitted to the adjacent perovskite slabs, which accommodate the distortion by adopting the same periodic corrugation.

4.2. Discussion

The structure exhibits strong similarities with the parent compound $Sr_4Fe_6O_{13-\delta}$. As a reminder, this phase has been described as an intergrowth of a single perovskite layer with an oxygen-deficient rock-salt-type layer, giving rise to three distinct coordination environments for the Fe atoms within the oxygen-deficient block, namely tetragonal pyramidal (TP), tetrahedral (T) and trigonal bipyramidal (TBP) sites. In the parent compound, however, the ordering of oxygen vacancies is incommensurate with the underlying lattice, resulting in an aperiodic succession of these coordination polyhedra. The modulation of the structure therefore directly originates from the distribution of oxygen vacancies within the rock-salt-type layer. In contrast, the Pb-containing phase investigated in the present work exhibits a fully periodic arrangement of the oxygen vacancies, giving rise to three Fe coordination environments following the sequence TP-T-TBP-TBP-T-TP, which is repeated throughout the structure. The introduction of Pb involves a long-range periodic ordering of the oxygen vacancies, leading to a commensurate modulation of the crystal structure. Such a stabilization of a commensurate modulated phase has also been reported in other members of this family, notably in the $m = 2$ compound containing double perovskite layers substituted with Bi (Lepoittevin *et al.*, 2004), and in the $m = 4$ compound containing quadruple perovskite layers doped with Tl (Lepoittevin, 2016).

A further structural comparison can be carried out with the Pb-containing ferrate $Pb_4Sr_2Fe_6O_{15}$ (Fig. S2), which also adopts an oxygen-deficient perovskite-related framework (Raynova-Schwarten *et al.*, 1997). However, the way in which the oxygen-deficient and perovskite layers are arranged differs between the two structures. $Pb_4Sr_2Fe_6O_{15}$ can be described as a regular intergrowth along the *c* axis of a double perovskite layer [$Sr_2Fe_2O_6$], with a single oxygen-deficient layer [$Sr_2Fe_2O_4$]. Within the latter, oxygen vacancies give rise to edge-sharing FeO_5 square pyramids, which form chains that are interconnected through FeO_6 octahedra. In contrast, in $Pb_4Sr_{14}Fe_{23}O_{52}$, the presence of Pb induces a collapse of the two types of layers, resulting in a structural arrangement comprising an oxygen-deficient double Fe layer associated with a single perovskite-type layer. The ordered distribution of oxygen vacancies gives rise to three distinct Fe environments, namely tetragonal pyramidal, tetrahedral and trigonal

bipyramidal, arranged in a periodic sequence. This collapse of the perovskite and oxygen-deficient layers modifies the stacking sequence and breaks the higher symmetry of the parent layered arrangement, thereby, giving rise to a monoclinic symmetry. Thus, although both structures can be understood in terms of intergrowth of oxygen-deficient and perovskite-type layers, the incorporation of Pb results in a fundamentally different periodic arrangement of these layers and of the oxygen vacancies.

5. Conclusion

In this study, the crystal structure of the ferrite $Pb_4Sr_{14}Fe_{23}O_{52}$ synthesized in 2006 has been finally successfully solved by 3D ED combined with atomic resolution STEM imaging. The structural model refined using the dynamical theory consists of a sheared layered framework resulting from the ordered incorporation of Pb atoms. The structure consists of the periodic collapse of two distinct structural blocks: a single perovskite layer and an oxygen-deficient rock-salt-type layer. Within the latter, the ordered distribution of oxygen vacancies gives rise to a regular sequence of Fe coordination polyhedral (TP-T-TBP-TBP-T-TP) and induces the characteristic corrugation of the layered framework. Bond valence sum calculations further indicate that most Fe atoms are trivalent, whereas the square pyramidal Fe site located adjacent to the Pb atoms exhibits an oxidation state close to Fe^{2+}, highlighting the strong influence of the local environment created by the Pb-induced collapse. The structure exhibits similarities with the parent phase $Sr_4Fe_6O_{13-\delta}$, but in contrast to this one the modulation appears to be commensurate, revealing an ordering of the oxygen vacancies. This feature was already observed in the Bi- and Tl-doped compounds, suggesting that these cations play a key role in promoting long-range ordering of oxygen vacancies and superstructures stabilization. Comparison with $Pb_4Sr_2Fe_6O_{15}$ highlights the structural role of Pb, as the two compounds exhibit on the one hand distinct arrangements of the oxygen-deficient and perovskite layers, and on the other hand different oxygen vacancies ordering. This work finally shows the efficiency of combining 3D ED with aberration-corrected STEM imaging for the determination of complex oxide structures.

Acknowledgements

The author thanks Dr Olivier Leynaud for the fruitful discussions and his precious help in the structure resolution. The author thanks also Professor Maryvonne Hervieu and Professor Sylvie Malo for providing the sample to study.

References

Brown, I. D. & Altermatt, D. (1985). *Acta Cryst.* B**41**, 244–247.
Clabbers, M. T. B., Gruene, T., Parkhurst, J. M., Abrahams, J. P. & Waterman, D. G. (2018). *Acta Cryst.* D**74**, 506–518.
Doyle, P. A. & Turner, P. S. (1968). *Acta Cryst.* A**24**, 390–397.
Gemmi, M., Mugnaioli, E., Gorelik, T. E., Kolb, U., Palatinus, L., Boullay, P., Hovmöller, S. & Abrahams, J. P. (2019). *ACS Cent. Sci.* **5**, 1315–1329.
Gorelik, T., Latychevskaia, T., Senkovska, I., Maliuta, M., Kaskel, S. & Kaiser, U. (2026). *Micron* **201**, 103960.
Grebille, D., Lepoittevin, C., Malo, S., Pérez, O., Nguyen, N. & Hervieu, M. (2006). *J. Solid State Chem.* **179**, 3849–3859.
Hervieu, M., Caldes, M. T., Cabrera, S., Michel, C., Pelloquin, D. & Raveau, B. (1995). *J. Solid State Chem.* **119**, 169–175.
Hervieu, M., Pérez, O., Groult, D., Grebille, D., Leligny, H. & Raveau, B. (1997). *J. Solid State Chem.* **129**, 214–222.
Huang, Z., Ge, M., Carraro, F., Doonan, C., Falcaro, P. & Zou, X. (2021). *Faraday Discuss.* **225**, 118–132.
Jansen, J., Tang, D., Zandbergen, H. W. & Schenk, H. (1998). *Acta Cryst.* A**54**, 91–101.
Kabsch, W. (2010). *Acta Cryst.* D**66**, 125–132.
Kanowitz, S. M. & Palenik, G. J. (1998). *Inorg. Chem.* **37**, 2086–2088.
Klar, P. B., Krysiak, Y., Xu, H., Steciuk, G., Cho, J., Zou, X. & Palatinus, L. (2023). *Nat. Chem.* **15**, 848–855.
Lepoittevin, C. (2016). *J. Solid State Chem.* **242**, 228–235.
Lepoittevin, C., Malo, S., Hervieu, M., Grebille, D. & Raveau, B. (2004). *Chem. Mater.* **16**, 5731–5735.
Lepoittevin, C., Malo, S., Pérez, O., Nguyen, N., Maignan, A. & Hervieu, M. (2006). *Solid State Sci.* **8**, 1294–1301.
Li, Y., Ling, Y. & Ma, Y. (2024). *Chin. J. Struct. Chem.* **43**, 100237.
Mei, K., Zhang, K., Xu, J. & Zhou, Z. (2023). *Crystals* **13**, 924.
Mellenne, B., Retoux, R., Lepoittevin, C., Hervieu, M. & Raveau, B. (2004). *Chem. Mater.* **16**, 5006–5013.
Mugnaioli, E., Gorelik, T. & Kolb, U. (2009). *Ultramicroscopy* **109**, 758–765.
Örs, T., Deroche, I., Chatelard, C., Dodin, M., Martinez-Franco, R., Tuel, A. & Paillaud, J.-L. (2024). *Symmetry*, **16**, 477.
Palatinus, L. (2013). *Acta Cryst.* B**69**, 1–16.
Palatinus, L., Brázda, P., Boullay, P., Perez, O., Klementová, M., Petit, S., Eigner, V., Zaarour, M. & Mintova, S. (2017). *Science* **355**, 166–169.
Palatinus, L., Brázda, P., Jelínek, M., Hrdá, J., Steciuk, G. & Klementová, M. (2019). *Acta Cryst.* B**75**, 512–522.
Palatinus, L. & Chapuis, G. (2007). *J. Appl. Cryst.* **40**, 786–790.
Palatinus, L., Petříček, V. & Corrêa, C. A. (2015). *Acta Cryst.* A**71**, 235–244.
Pennycook, S. J., Rafferty, B. & Nellist, P. D. (2000). *Microsc. Microanal.* **6**, 343–352.
Pérez, O., Mellenne, B., Retoux, R., Raveau, B. & Hervieu, M. (2006). *Solid State Sci.* **8**, 431–443.
Petříček, V., Palatinus, L., Plášil, J. & Dušek, M. (2023). *Z. Kristallogr. Cryst. Mater.* **238**, 271–282.
Plana-Ruiz, S., Götz, E., Neumann, T., Schwesig, P. & Kolb, U. (2024). *Acta Cryst.* B**80**, 105–116.
Raynova-Schwarten, V., Massa, W. & Babel, D. (1997). *Z. Anorg. Allg. Chem.* **623**, 1048–1054.
Tirado, J. I., Das, P. P., Jordá, J. L., Palatinus, L., Plana-Ruiz, S., Simancas, J., Simancas, R., Nicolopoulos, S., Valencia, S. & Rey, F. (2025*a*). *Microporous Mesoporous Mater.* **382**, 113392.
Tirado, J. I., Sala, A., Bordes, A., Pratim Das, P., Palatinus, L., Nicolopoulos, S., Jordá, J. L., Vidal–Moya, A., Blasco, T., Sastre, G., Valencia, S. & Rey, F. (2025*b*). *Angew. Chem. Int. Ed.* **64**, e202416515.
Wan, W., Sun, J., Su, J., Hovmöller, S. & Zou, X. (2013). *J. Appl. Cryst.* **46**, 1863–1873.
Yang, T., Xu, H. & Zou, X. (2022). *J. Appl. Cryst.* **55**, 1583–1591.
Yörük, E., Brázda, P. & Palatinus, L. (2025). *J. Mol. Struct.* **1343**, 142798.
Zhou, Z., Palatinus, L. & Sun, J. (2016). *Inorg. Chem. Front.* **3**, 1351–1362.